Theoretical and Applied Mechanics Letters 13 (2023) 100452

Contents lists available at ScienceDirect

Theoretical and Applied Mechanics Letters

journal homepage: www.elsevier.com/locate/taml

Assessment of the stiffened panel performance in the OTEC seawater tank design: Parametric study and sensitivity analysis

Yogie Muhammad Lutfi[a], Ristiyanto Adiputra[b,*], Aditya Rio Prabowo[a,*], Tomoaki Utsunomiya[c], Erwandi Erwandi[b], Nurul Muhayat[a]

[a] Department of Mechanical Engineering, Universitas Sebelas Maret, Surakarta 57126, Indonesia
[b] Research Center for Hydrodynamics Technology, National Research and Innovation Agency (BRIN), Surabaya 60117, Indonesia
[c] Department of Marine Systems Engineering, Kyushu University, Fukuoka 819-0395, Japan

ARTICLE INFO

Article history:
Received 21 January 2023
Revised 31 March 2023
Accepted 5 April 2023
Available online 6 April 2023

Keywords:
Ocean thermal energy conversion (OTEC)
Seawater tank
Stiffened panels
Numerical analysis
Combined loadings

ABSTRACT

Ocean thermal energy conversion (OTEC) is a process of generating electricity by exploiting the temperature difference between warm surface seawater and cold deep seawater. Due to the high static and dynamic pressures that are caused by seawater circulation, the stiffened panel that constitutes a seawater tank may undergo a reduction in ultimate strength. The current paper investigates the design of stiffening systems for OTEC seawater tanks by examining the effects of stiffening parameters such as stiffener sizes and span-over-bay ratio for the applied combined loadings of lateral and transverse pressure by fluid motion and axial compression due to global bending moment. The ultimate strength calculation was conducted by using the non-linear finite element method via the commercial software known as ABAQUS. The stress and deformation distribution due to pressure loads was computed in the first step and then brought to the second step, in which the axial compression was applied. The effects of pressure on the ultimate strength of the stiffener were investigated for representative stiffened panels, and the significance of the stiffener parameters was assessed by using the sensitivity analysis method. As a result, the ultimate strength was reduced by approximately 1.5% for the span-over-bay ratio of 3 and by 7% for the span-over-bay ratio of 6.

Concerns about the importance of green energy have grown in recent decades, as the threats of global warming have become widespread. Wet areas are becoming wetter, and dry areas are becoming drier [1]. Droughts are threatening crops and causing a freshwater deficit problem. Unexpected floods are devastating buildings and infrastructure. Not only has climate change provoked both a global environmental transformation and financial crisis [2–7], but it also threatens people's sovereignty and livelihood [8]. Attempts to reduce carbon emissions have been made all over the world. Global commitment to the cause has also been ratified [9]. Nonetheless, considering the impacts of global warming which have already arisen, these efforts must be progressed more significantly. All alternatives, including the rapid conversion of fossil-based energy to renewable energy [10–14], should be considered. However, despite its enormous potential and benefits, the technology for specific renewable energy resources such as ocean thermal energy conversion (OTEC) is not mature enough for commercial-scale usage [15,16]. In response to the aforementioned issue, the current paper seeks to improve the technical readiness of OTEC technology.

OTEC is a method of harvesting solar energy that is stored in the ocean. The system uses the temperature difference between cold deep seawater and warm surface seawater to form and reform the phases of the working fluid [17]. Several models of OTEC systems have been developed to increase the efficiency of the systems; the well-known models among them are the open cycle, closed cycle, and hybrid systems. A comprehensive review of this topic can be found in Ref. [18]. In brief, the open cycle system utilizes warm seawater directly to produce electricity; the closed cycle system transfers the heat energy of the warm seawater to the working fluid with a low boiling temperature. However, the hybrid system combines the principal mechanisms of the open and closed cycle. Because of its safety, cost-effectiveness, and efficiency, the

* Corresponding authors.
E-mail addresses: ristiyanto.adiputra@brin.go.id (R. Adiputra), aditya@ft.uns.ac.id (A.R. Prabowo).

https://doi.org/10.1016/j.taml.2023.100452

Nomenclature

A	net sectional area of the stiffened panel, cm^2
A_p	net sectional area of the attached plating, cm^2
A_{pE}	effective area of the plate, cm^2
A_s	net sectional area of the stiffener, cm^2
a	ordinary stiffener spacing, m
B_0	maximum amplitude of initial imperfection for column and torsional buckling mode
b	distance of the transverse stiffener, m
b_E	effective width of the stiffener, mm
b_f	width of the flange, mm
E	Young's modulus, MPa
h_w	net web height, mm
h_{we}	effective height of the stiffener, mm
I	Second moment inertia of area, m^4
L_{FEM}	length of the FEM model of the stiffened panel
R_{eHp}	minimum yield stress, N/mm^2, of the plate
R_{eHs}	minimum yield stress, N/mm^2, of the stiffener
t_f	thickness of the flange, mm
t_w	thickness of the web, mm
W_0	maximum amplitude of the initial imperfection for local buckling mode
β_E	effective plate slenderness
β_p	plate slenderness
$\sigma_{C1,2}$	critical stress, N/mm^2 for each respective buckling mode, MPa
$\sigma_{CR\ 1}$	ultimate strength of the stiffened panel under column buckling, MPa
$\sigma_{CR\ 2}$	ultimate strength of the stiffened panel under torsional buckling, MPa
$\sigma_{CR\ 3}$	ultimate strength of the stiffened panel under web local buckling, MPa
σ_Y	yield strength of the material, MPa
Φ	edge function

closed cycle system is preferred and has become primarily a case study of previous studies [19–21].

Fig. 1 depicts the schematic of the closed OTEC system. In this case, the working fluid is ammonia. First, ammonia is pumped into the evaporator to change the phase of the ammonia from liquid to gas by using heat from warm surface seawater. The vaporized ammonia is then used to rotate the turbine and generate electricity. The low-pressure ammonia is then delivered to the condenser to be converted to the liquid phase by using cold deep seawater. To repeat the cycle continuously, the liquid ammonia is pumped back into the evaporator [17,22].

The value of OTEC exploration is undeniable. Not only does the OTEC system generate electricity, but it also provides additional benefits such as water desalination for freshwater supply, the cultivation of marine organisms by utilizing nutrient-rich deep seawater, and an air-conditioning system [23]. The resource of OTEC energy is stable, free, and abundantly available and can be harvested throughout the year. When the additional benefits are taken into account and the scale of production is increased, the OTEC industries are comparable to those of other renewable energy resources [24]. Even though the potential of this technology is huge, the necessity is urgent, and the demand is high, OTEC development is not remarkable when compared to that of other renewable energy sources. There are many reasons for this phenomenon, but the root of these reasons is the same in that it results from the low efficiency of OTEC. The OTEC system relies solely on the temperature difference between warm surface seawater and cold deep seawater. With a temperature gradient of 20 °C between seawater temperatures at depths of 50 and 1000 m, the net thermal efficiency is less than 5% [25]. Thus, the amount of warm surface seawater and cold deep seawater required to produce electricity on a commercial scale would be very large. Consequently, the design of the pipes to transport the seawater and the tank for storage must be not only innovative but also massive in size. Briefly, the OTEC system is very simple and applicable, but the supporting structure still requires further research and development. Several studies have been published on the pipe that is used to transport deep seawater to the board cold-water pipe (CWP). Adiputra and Utsunomiya [26] investigated the stability of the CWP due to the internal flow. The an-

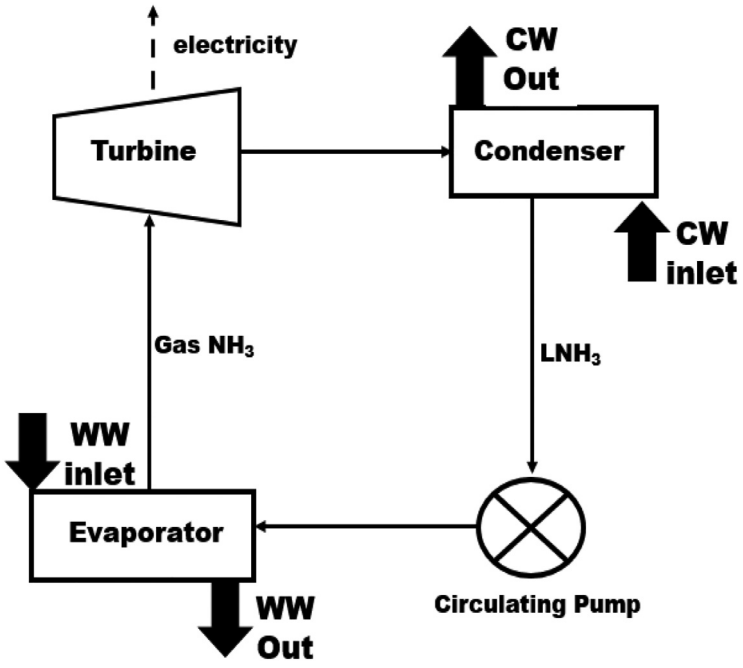

Fig. 1. Schematic of OTEC closed system.

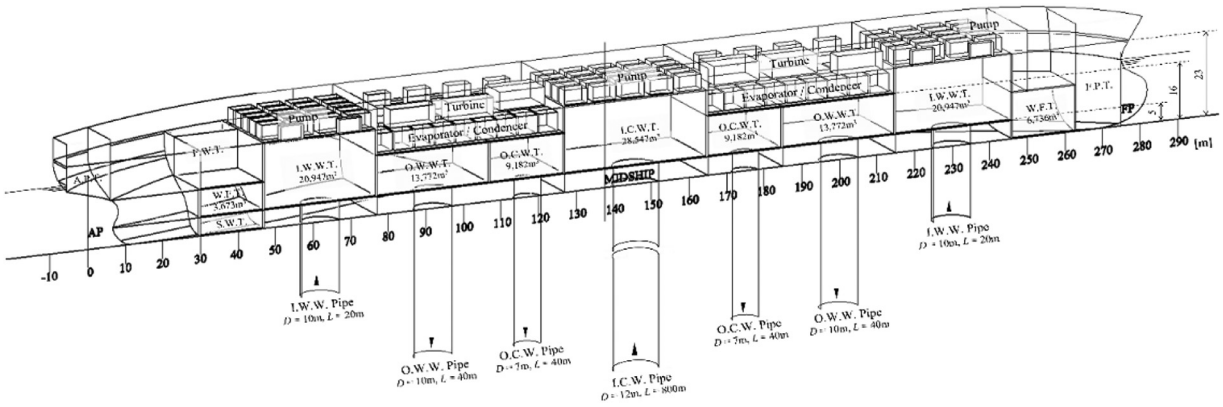

Fig. 2. OTEC plantship layout from oil tanker conversion (Hisamatsu and Utsunomiya [32]).

alytical formulation was then expanded in Refs. [27,28] by varying the prospective CWP and the inclusion of alternative mathematical solutions. OTEC CWP Finite Element modeling has also been proposed by Ref. [29] to assess the CWP stability in time domain analysis. Hisamatsu and Utsunomiya [30] investigated the coupled motion of the CWP and the plantship. A series of experiments on a fluid conveying pipe was also carried out in Ref. [31].

A review of the literature on the seawater tank yields very few resources. The requirements and significance of installing a seawater tank were highlighted in Refs. [17,32]. Seawater tank size optimization has been conducted based on the applied pressure, but its response to the structural integrity has not yet been considered. In this paper, the stiffening system of the seawater tank design is thoroughly analyzed by varying its parameters and assessing their influence on the ultimate strength of the panel.

As previously indicated, OTEC technology is still in its infancy. Although a number of pilot projects have been developed successfully, the practicality of OTEC on a larger scale is still unclear. There are still many factors that need to be clarified. The key issues are how large of a scale should be used to render this technology profitable and how to lower capital costs [24]. According to economic research on OTEC, efficiency increases with a greater temperature difference between the deep ocean and the surface layer [33,34]. The cost of electricity will decrease as targeted net-power output increases, making this form of technology more competitive [20,24]. Following this, the commercial scale of the OTEC plant becomes the target of development [22,35,36]. The OTEC plant can be installed either on- or offshore. The on-shore option is preferable for pilot projects due to the ease of installation and fabrication. Furthermore, because the purpose of the pilot project is to conduct research and development, an offshore plant is more convenient. However, on a commercial scale, as the required deep seawater becomes greater, and the cold-water pipe becomes bigger, the offshore plant presents a better option. Several previously published papers or project reports on the plantship design for commercial OTEC have been mentioned in the introductory section of Adiputra et al. [22]. The reports were conducted mostly by engineering firms and did not provide much detailed information. Adiputra et al. [22] conceptualized and designed an OTEC plantship by using ship conversion from an oil tanker ship with some consideration that to some extent, an oil tanker ship has the most similar characteristics to those of an OTEC plantship, such as the existence of such tanks to store fluids. The use of ship conversion itself was intended to reduce capital costs. To the best of the author's knowledge, no publications on significant improvements to the conceptual design have been developed since then.

The ship-shape OTEC platform offers advantages in allocating the area for the OTEC system equipment and volumetric space for the fluid tank for the seawater and working fluid. The motion of ship-shape offshore structures is also more stable compared with that of other types of offshore structures. For yielding 100 MW net electricity, the results from Adiputra et al. [22] stated that the size of the oil tanker ship should be approximately that of the typical Suez max oil tanker. The main dimensions of the proposed plantship are listed in Table 1. The proposed general arrangement of the plantship was visualized in a three-dimensional format by Hisamatsu and Utsunomiya [32], as shown in Fig. 2.

Table 1
Main dimension of OTEC plantship from oil tanker ship conversion (Adiputra et al. [22]).

Parameter	Scantlings	Parameter	Scantlings
Length overall (m)	285	Draft (m)	
Breadth (m)	30	Block coefficient	0.84
Height (m)	30	Seawater velocity (m/s)	

As seen in Fig. 2, the characteristics of the OTEC plantship rely on a required additional structure to support and maintain the OTEC cycle. The seawater pipes are required to discharge or deliver the seawater to the board and vice versa. Storage tanks include the inlet and outlet cold-water tanks, the inlet and outlet warm-water tanks, and a tank for the working fluid separator and reservoir.

The function of seawater tanks is to store seawater before it is delivered to the heat exchanger. The function of these tanks is also to allow seawater to move freely when the plantship is in motion, particularly when it is subjected to heave motion. Without the tank, the valve would be vulnerable due to excessive pressure. Fig. 3 shows the conceptual design of OTEC seawater tanks extracted from Fig. 2. At the bottom, there is a joint connection

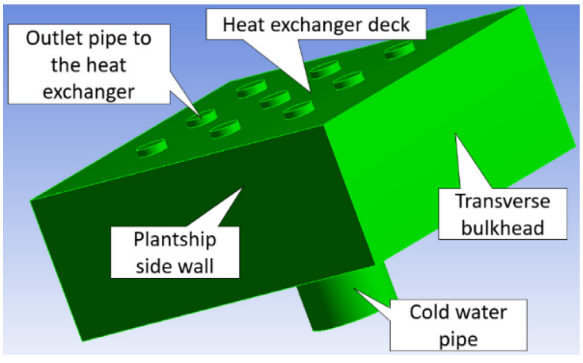

Fig. 3. Schematic of OTEC closed system. (For interpretation of the references to color in this figure legend, the reader is referred to the web version of this article.)

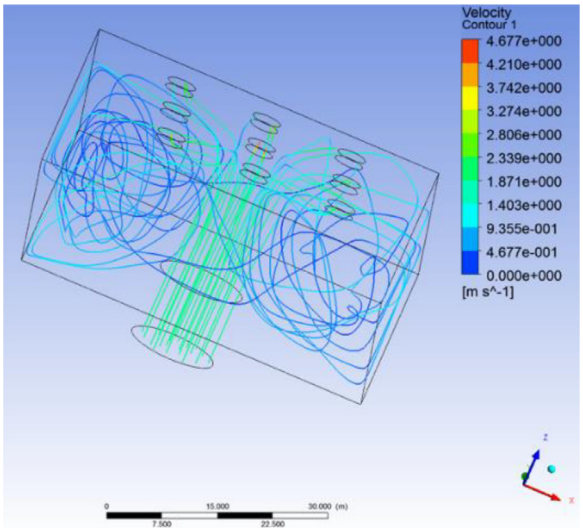

Fig. 4. Velocity distribution inside the seawater tank. (For interpretation of the references to color in this figure legend, the reader is referred to the web version of this article.)

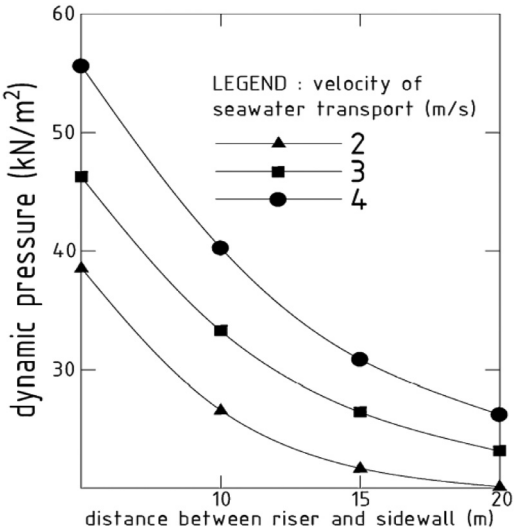

Fig. 5. Dynamic pressure on the side tank wall [22].

between the plantship and seawater pipes. The port and starboard sides of the tank are the plantship hull. The front and back sides are the compartment bulkhead. The top deck is allocated for the heat exchanger compartment. The seawater tank and the cold-water pipe are set to be at the midship region to maintain the stability of the plantship and avoid extreme trim conditions.

The seawater comes from the inlet and is then delivered to the heat exchanger through the outlet pipe. The incoming debit of seawater is equal to the debit of seawater transferred to the heat exchanger, based on mass balance. As the flow is not steady and the flow field is random, turbulence takes place inside the seawater tank. Fig. 4, which was produced by using the commercial software ANSYS interface, shows the sample of the velocity distribution inside the tank with a velocity of 2 m/s at the inlet.

As shown in Fig. 4, the near-wall velocity distribution of seawater is not equal, and there is an attack angle between the velocity direction and the tank walls. These conditions cause dynamic pressure that acts on the side wall, as shown in Fig. 5 for various seawater transport velocities [22]. Even though seawater transport of 2–3 m/s is preferable considering the energy loss of the pump and the system stability, for cautious investigation, a dynamic motion of 0.06 MPa resulting from a seawater velocity of 4 m/s is chosen in this present paper to account for an undesirable condition. The observed point is around the corner between the side wall and the top deck, as the maximum dynamic pressure was observed there. Assuming a distance of 10 m between the observed point and the seawater level, the static pressure of 0.1 MPa can be derived. A total pressure load of 0.16 MPa is obtained.

As part of the plantship structure, the seawater tank is also subjected to global loads. Because of its relatively long length, a ship-shaped floating structure is subjected to a significant longitudinal bending moment. The longitudinal bending moment generally refers to the summation of the still-water and the wave-induced bending moment. The still-water bending moment is caused by the uneven distribution of the plantship weight across the buoyancy. Moreover, the wave-induced bending moment is caused by the wave motion, which makes the buoyancy along the ship drastically unequal.

Longitudinal plantship deformation that is caused by longitudinal bending is classified into two conditions. In the hogging condition, the deck part of the plantship is subjected to tension, whereas the bottom part is subjected to compression, and vice versa in the sagging condition. Fig. 6 schematically shows the process of the global bending moment in sagging conditions and its influences on the seawater tank structure. When the peak of the wave is located in the fore and after part of the plantship, the buoyancy in those regions is higher than in the amidship region. Consequently, the top part of the seawater tank, which is above the neutral axis of the ship, is compressed, whereas the bottom part is tensed. Ac-

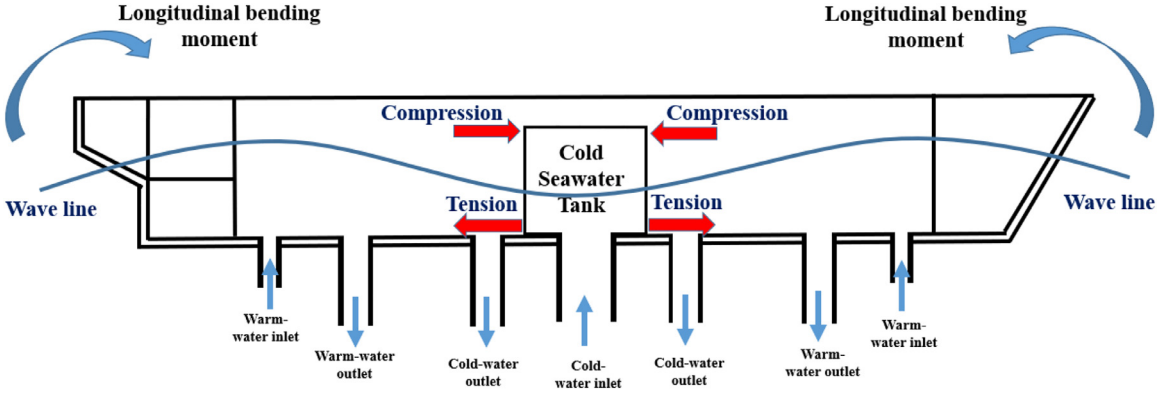

Fig. 6. Schematic of longitudinal bending moment and the OTEC seawater tank responses. (For interpretation of the references to color in this figure legend, the reader is referred to the web version of this article.)

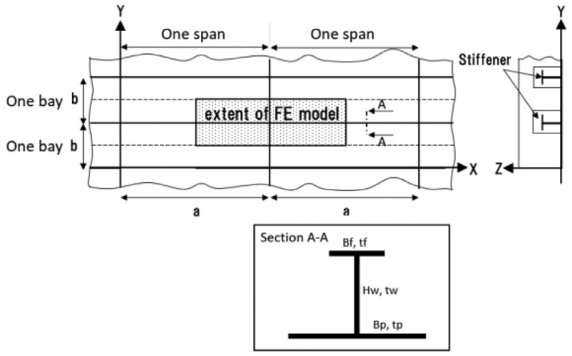

Fig. 7. Extended region of the observed stiffened panel as part of the grillage of the seawater tank. (For interpretation of the references to color in this figure legend, the reader is referred to the web version of this article.)

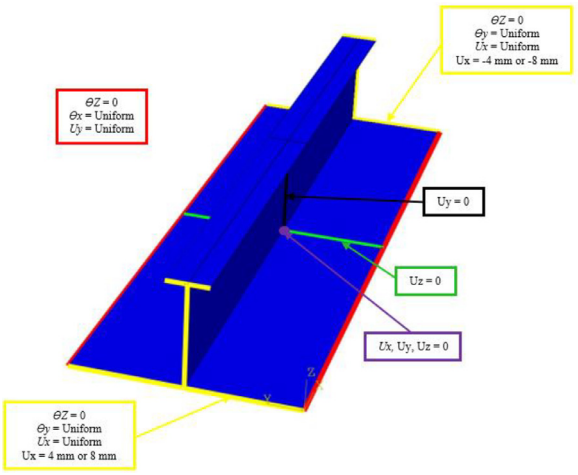

Fig. 8. Boundary conditions for FEM analysis. (For interpretation of the references to color in this figure legend, the reader is referred to the web version of this article.)

cording to beam theory, the maximum stress that is caused by the longitudinal bending moment is located near the midship, where the cold seawater tank is located. Thus, the cold seawater tank bears the maximum stress due to bending compared to the other seawater tanks.

In brief, the seawater tank which is installed to maintain a continuous supply of cold and warm seawater to the heat exchanger is subjected to hydrostatic pressure due to ambient fluid and dynamic pressures due to seawater circulation. Because of the pressure loads, the stiffened panel that constitutes the seawater tank may undergo a reduction in ultimate strength when the global bending moment occurs, potentially resulting in structural failure. To ensure the structural integrity of the seawater tank, the condition of seawater tanks which are subjected to combined pressure and axial compression loads must be considered when designing the stiffening system. However, because the OTEC plantship is still in early development, there is no specific design code or regulation for the stiffening system of such tanks. The current study examines the effect of pressure loads (lateral and transverse pressure) on the ultimate strength of stiffened panel elements that are used in the structure of a seawater tank by conducting the non-linear finite element method with two dependent load steps. The scantlings of the stiffened panel model are proposed based on the typical stiffened panel of the cargo tank in an oil tanker ship. The significance of the stiffening parameter is also assessed by conducting a parametric study of the stiffened panel scantling and optimization based on the yield stress reduction in the designed stiffened panel.

Analyzing the full size of the seawater tank is very time-consuming and requires a high computational capacity, especially when it comes to a parametric study in which many parameters have to be varied, and simulation should be performed repeatedly. Thus, in the present study, instead of analyzing a full-scale tank, the effect of the pressure load on the structure of the stiffened panels that constitute a seawater tank was analyzed. This procedure was suitable considering that a seawater tank, as part of a plantship, has primary support members such as girders and transverse webs, which are stiff enough to prevent the overall buckling in such a way that only local buckling and yielding of stiffeners may take place. Thus, the effects of pressure load on the stiffened panel that constitutes a seawater tank are proportional to the seawater tank as a whole. Fig. 7 shows the sketch of the grillage of the wall of the seawater tank. The analyzed stiffened panel was hatched in the gray region covering the ½+½ bay and ½+½ span, as was also the case in Ref. [37]. The main scantling parameters of the stiffened panels, as illustrated in section A–A, include the thickness and breadth of the plate, the height and thickness of the web, and the breadth and thickness of the flange.

The base scantling of the model was adapted from the typical stiffener size of a cargo hold in an ultra-large crude carrier oil tanker [38]. This approach was based on the consideration that the designed plantship was converted from such a ship [39]. A stiffened panel in the cargo hold of tanker ships is also subjected to fluid pressure, as in the OTEC seawater tank. In the simulation, the span-over-bay ratio was assumed to be between 3 and 6. The thickness and breadth of the base plate and flange were fixed. The plate thickness was set to the maximum thickness on the ship hull of 25 mm. The breadth of the base plate was set to 800 mm, which is the length of 1 transverse span. The breadth of the flange, b_f, was set to 150 mm, which is approximately 1/3 of the web height. The web height, h_w, was varied to 400 mm, 450 mm, and 500 mm to examine the effect of stiffener inertia on the reduction in ultimate strength. The thickness of the web, t_w, was set to 11 and 12 mm, whereas the thickness of the flange, t_f, was set to 22, 25, and 28 mm, respectively. Table 2 contains the detailed case configuration.

The case configuration is numbered in order of the three varied parameters. The first order denotes the web height variations of 400 mm, 450 mm, and 500 mm as hw1, hw2, and hw3, respectively. The second order denotes the variations in web thickness of 11 mm and 12 mm as tw1 and tw2, respectively. The third order denotes the variation in flange thickness as tf1, tf2, and tf3. Case hw2tw1tf3, for example, refers to a stiffened panel with a web height of 450 mm, a web thickness of 11 mm, and a flange thickness of 28 mm.

In order to obtain accurate results and portray the buckling behavior of the stiffened panel, the numerical simulation must be carried out cautiously. In the present study, the simulation was conducted by using a non-linear finite element analysis via ABAQUS [40]. The boundary condition of the present study, which followed the principle of boundary condition by Adiputra et al. [39], is shown in Fig. 8. To embody the effect of the structural response of the surrounding stiffened panels on the observed ones, the continuous boundary condition along the longitudinal and transverse edges of the base plate was considered.

In the simulation, the transverse stiffener was not geometrically modeled to simplify the modeling effort, but its contribution to the structural integrity was considered by imposing zero displacements on the element where the transverse stiffener was located (lateral displacement for the base plate and transverse displacement for the web). The imposed displacement was set to be 4 mm for the span-over-bay ratio of 3 and 8 mm for the span-over-bay

Table 2
Case configuration of the scantlings of the analyzed stiffened panels in mm.

Case no.	Web		Flange		Case no.	Web		Flange		Case no.	Web		Flange	
	h_w	t_w	b_f	t_f		h_w	t_w	b_f	t_f		h_w	t_w	b_f	t_f
hw1tw1tf1	400	11	150	22	hw2tw1tf1	450	11	150	22	hw3tw1tf1	500	11	150	22
hw1tw1tf2	400	11	150	25	hw2tw1tf2	450	11	150	25	hw3tw1tf2	500	11	150	25
hw1tw1tf3	400	11	150	28	hw2tw1tf3	450	11	150	28	hw3tw1tf3	500	11	150	28
hw1tw2tf1	400	12	150	22	hw2tw2tf1	450	12	150	22	hw3tw2tf1	500	12	150	22
hw1tw2tf2	400	12	150	25	hw2tw2tf2	450	12	150	25	hw3tw2tf2	500	12	150	25
hw1tw2tf2	400	12	150	28	hw2tw2tf2	450	12	150	28	hw3tw2tf2	500	12	150	28

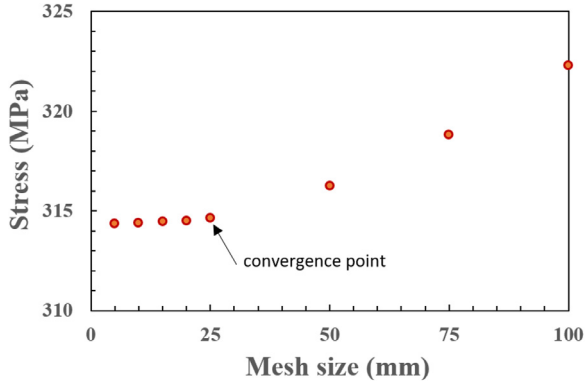

Fig. 9. Mesh convergence trends: the convergence is achieved in a mesh range between 0 and 25 mm. (For interpretation of the references to color in this figure legend, the reader is referred to the web version of this article.)

ratio of 6. The imposed displacement was determined by considering the strain yield, which was calculated based on the material properties of the panels with Young's modulus of 205,800 MPa and yield strength of 352 MPa.

To determine the appropriate mesh size, a mesh convergence study was carried out as shown in Fig. 9. From Fig. 9, it can be concluded that the simulation reached the convergence value at a mesh size of 25 mm. Thus, the meshing was set to be uniform with an element length of 25 mm, as shown in Fig. 10, which is also in agreement with a previously published paper [37].

To consider the geometrical imperfection that is caused by the manufacture and production process, the coordinates of all nodes were modified based on three possible buckling modes, as listed in Eqs. (1)–(3) for column buckling, torsional buckling, and local buckling, respectively, which were obtained from [39].

$$w_{0column} = B_0 \sin\frac{\pi x_i}{a}, \tag{1}$$

$$w_{0torsional} = B_0 \frac{z_i}{hs} \sin\frac{\pi x_i}{a}, \tag{2}$$

$$w_{0local} = C_0 \sin\frac{m\pi x_i}{a} \sin\frac{\pi y_i}{b}, \tag{3}$$

where

$$B_0 = L_{FEM}/1000, \tag{4}$$

$$C_0 = 0.1\ \beta_p^2 t \qquad \text{in which} \qquad \beta_p = \frac{b}{t_p}\sqrt{\frac{\sigma_y}{E}}. \tag{5}$$

x_i, y_i, z_i are coordinates of the node in the X-axis, Y-axis, and Z-axis, respectively; a is the span length that is equal to the distance of the longitudinal stiffener; b is the bay length that is equal to the distance of the transverse stiffener; and L_{FEM} is the length of the stiffened model.

Table 3
Ultimate strength of the stiffened panel (in MPa).

Method	Buckling modes	Designed cases		
		hw1tw1tf1	hw2tw1tf2	hw3tw2tf3
IACS-CSR	Column	344.71	345.78	346.58
	Torsional	336.79	334.37	331.95
	Local	345.39	342.19	340.78
FEM	Combination	329.636	331.2	332.96

Before conducting all case configurations, it is critical to ensure that the procedures in finite element modeling, from geometrical modeling to the result processing, are correct. The ultimate strength of the selected stiffened panels obtained through FEM was compared to that predicted by the IACS-CSR code for verification [41]. The pressure effect was not taken into account by the IACS-CSR. Thus, the first load step, which imposes the pressure load, was surpassed. The IACS-CSR predicts the ultimate strength of the stiffened panel by assuming the occurrence of three buckling modes, including the column buckling, torsional, and local buckling modes. The results were compared, and the ultimate strength was calculated by using the lowest value obtained. Eqs. (6)–(8) show the mathematical models for estimating ultimate strength based on the IACS-CSR for column, torsional, and local buckling modes, respectively.

$$\sigma_{CR\ 1} = \phi\sigma_{C1}\frac{A_{s+}A_{pE}}{A_{s+}A_p}, \tag{6}$$

$$\sigma_{CR2} = \phi\frac{A_s\sigma_{C2} + A_p\sigma_{CP}}{A_s + A_p}, \tag{7}$$

$$\sigma_{CR3} = \phi\frac{10^3 b_E t_p R_{eHp} + \left(h_{we}t_w + b_f t_f\right)R_{eHs}}{10^3 s t_p + h_{we}t_w + b_f t_f}. \tag{8}$$

The column buckling mode considers the response of the stiffened panel to the overall buckling based on the Euler beam theory. The torsional buckling takes into account the tripping load that acts on the stiffened panel, especially on the web part. The local buckling considers the partial collapse of the stiffened panel part due to the disproportional thickness of the panel elements.

Fig. 11 compares the ultimate strength of the stiffened panels based on the FEM and IACS-CSR code for three selected stiffened panels of hw1tw1tf1, hw2tw1tf2, and hw3tw2tf3. The panels were selected based on the proportional variation in web height, web thickness, and flange thickness. The stress strain behavior of these three models is relatively similar based on the FEM and IACS-CSR code, as shown in Fig. 11. Based on the IACS-CSR code, all selected panels collapse in the torsional buckling mode.

Based on Fig. 11, the ultimate strength of the stiffened panels can be obtained, as shown in Table 3. When the detailed figures of the peak stress–strain curve and the ultimate value stated in Table 3 are compared, there is an interesting thing to note. The results from the IACS-CSR code show that by increasing the

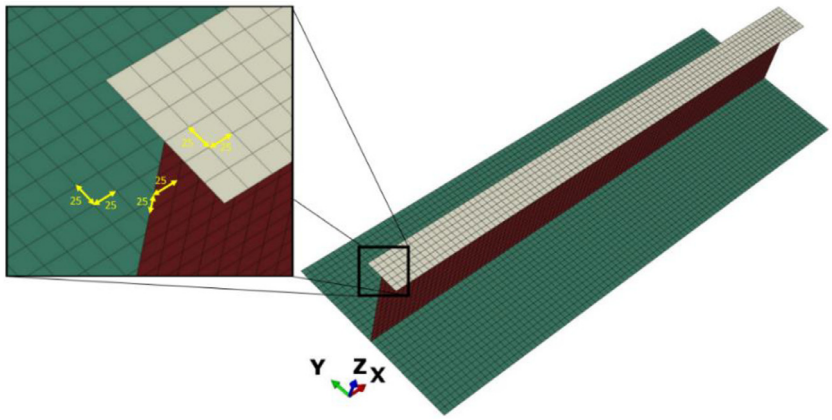

Fig. 10. Meshing of the model. (For interpretation of the references to color in this figure legend, the reader is referred to the web version of this article.)

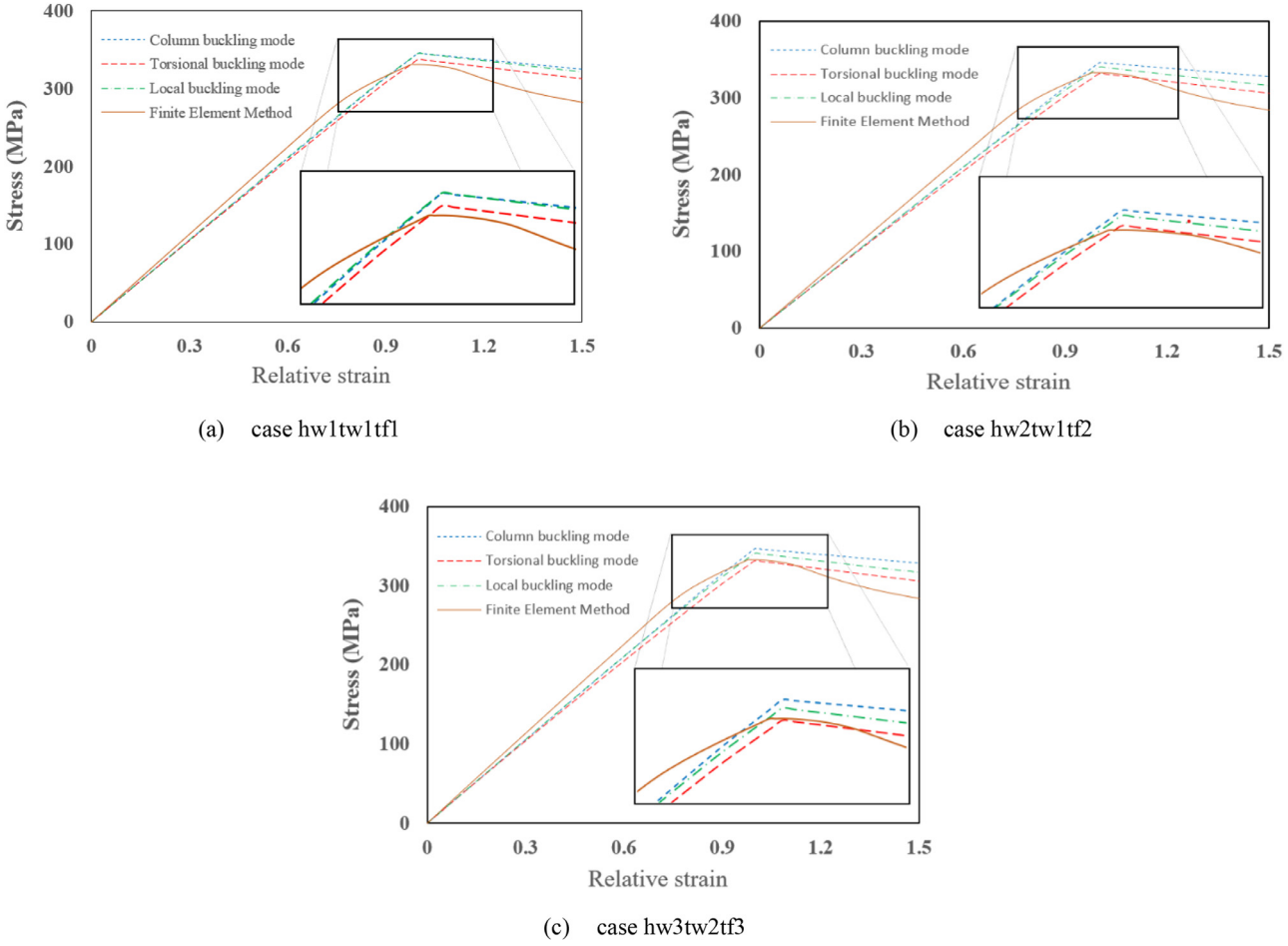

Fig. 11. Ultimate strength of selected stiffened model by FEM and IACS-CSR. (For interpretation of the references to color in this figure legend, the reader is referred to the web version of this article.)

height of the web (hw1-hw3), the ultimate strength that is predicted for the column buckling mode is increased, but vice versa for the torsional buckling mode. This is because the increase in web height will increase the moment inertia of the area of the stiffened panel and the stress–strain equation for the column buckling mode is proportional to it. However, in the torsional buckling mode, increasing the web height raises the Euler torsional buckling stress. Nevertheless, because the ultimate strength is determined by the minimum value of all buckling modes, the ultimate strength follows the predicted ultimate value for the torsional buckling mode.

The FEM results are similar to the ultimate strength predicted by IACS-CSR in the torsional buckling mode, but the ultimate strength is proportional to the web height increment, which differs from the tendency of the IACS-CSR results. FEM can account for the buckling mode interaction. Even though the torsional buckling mode dominates the collapse, the presence of the column buckling mode increases the ultimate strength. This phenomenon cannot be captured by using the IACS-CSR code.

Fig. 12 compares the stress–strain relationship of a stiffened panel hw1tw1tf1 with a span-over-bay ratio of six under axial compression and the combined loadings of pressure and axial

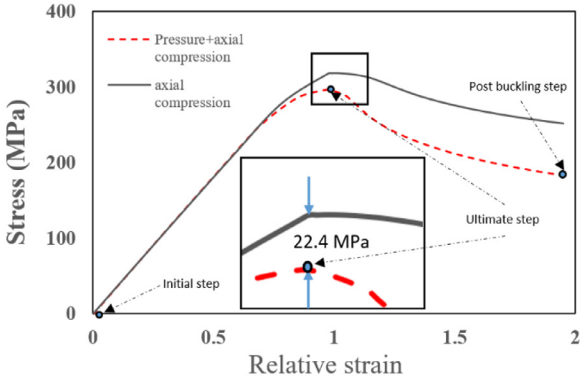

Fig. 12. Ultimate strength reduction due to pressure load. (For interpretation of the references to color in this figure legend, the reader is referred to the web version of this article.)

compression. In this particular step, the pressure value is set to be 0.16 MPa, which indicates the extreme condition. According to the graph, the pressure load reduces the ultimate strength by about 22.4 MPa, or about 7% of the ultimate strength. However, as shown in the scaled-up graph, the pressure load has no effect on the ultimate strain. However, in the post-buckling region, the reduction in stress is very sensitive to the progression or relative strain.

Figs. 13–15 portray the stress field and deflection in a specific axis of the stiffened panel during the remarkable simulation steps that are depicted in Fig. 12, including the initial condition, ultimate, and post-buckling steps. Fig. 13 shows the initial condition of the stress field and deflection of the stiffened panel right before the axial compression is progressed due to the applied pressure acting in the first load step. Because there is a fixed support that is contributed by the joint between the transverse and longitudinal stiffening systems at the mid-point of the stiffened panel, the deflection is close to zero, and as a result, the stress is concentrated around that point.

The deflected and stressed stiffened panel of Fig. 13 is then axially compressed via the displacement control method, in which the imposed displacement is progressed through the time step. Fig. 14 shows the stress distribution and the transverse displacement of the web in the ultimate condition. Based on the stress distribution in Fig. 14a, the panel is subjected to column buckling modes in which the plate, web, and flange reach the yield stress. By observing Fig. 14b, it can also be seen that the web and flange are deflected in a wave of the sinusoidal mode around the mid-section, indicating the occurrence of web torsional buckling. Thus, the collapse mode occurs as a combination of column and torsional buckling modes.

Fig. 15 captures the behavior of the panel after buckling. In contrast to the condition of the panel in the ultimate step, as shown in Fig. 15a, the stress becomes concentrated at the mid-point of the panels and is not evenly distributed between the front and back sides of the panel. It strongly indicates the existence of the torsional buckling mode, which is also shown in the transverse deflection of the panel, as in Fig. 15b. By incorporating Figs. 13–15, it can be concluded that while the axial compression is advanced, the column buckling mode takes place; however, once the panel reaches its ultimate capacity, torsional buckling takes over and becomes more dominant.

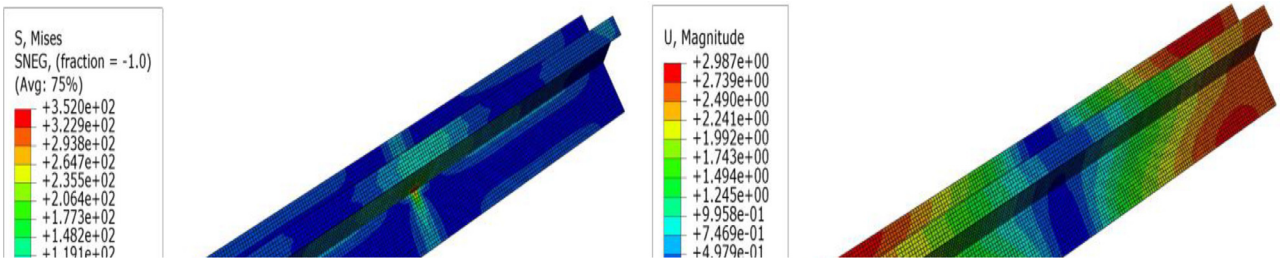

(a) Stress field (b) Deflection distribution

Fig. 13. Stress field and deflection distribution of the stiffened panel that is subjected to lateral and transverse pressure. (For interpretation of the references to color in this figure legend, the reader is referred to the web version of this article.)

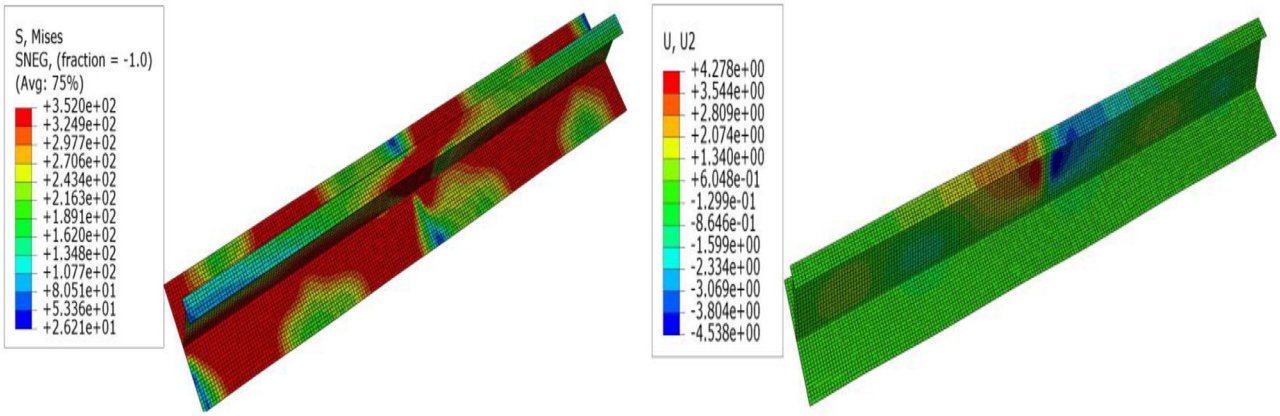

(a) Stress distribution (b) Transverse panel deflection

Fig. 14. Stress field and transverse deflection of the panel at the ultimate step. (For interpretation of the references to color in this figure legend, the reader is referred to the web version of this article.)

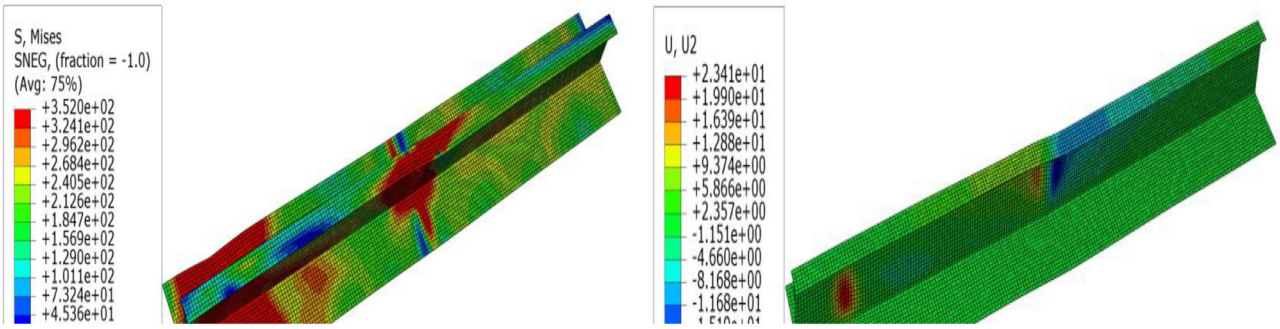

(a) Stress distribution (b) Transverse panel deflection

Fig. 15. Stress field and transverse deflection of the panel at the post-buckling step. (For interpretation of the references to color in this figure legend, the reader is referred to the web version of this article.)

Fig. 16 depicts the ultimate strength reduction as the pressure load increases. Three stiffened panels are used: hw1tw1tf1, hw2tw1tf2, and hw3tw2tf3. The pressure is raised from 0 MPa to 0.24 MPa in 0.4 MPa increments. In general, all selected models yield relatively the same trend line. When relatively small pressure loads are applied, the ultimate strength reduction is negative, indicating that the pressure load increases the ultimate strength. The explanation for this phenomenon can be found in Refs. [42,43]. However, after about 0.06 MPa of applied pressure load, the pressure begins to reduce the ultimate strength in a polynomial fashion, as shown by the regression line. Despite having the same tendency relatively, the sensitivity of those three panels toward the change in the pressure load is different. This trend is expected considering that the designated panels have different size parameters. A sensitivity analysis is carried out in the next subsection to ascertain which parameter may influence the yield strength reduction the most.

A sensitivity analysis is a method of observing how the targeted parameter, in this case, the ultimate strength of the stiffened panel, changes under the effect of other input parameters. The stiffened panel parameter refers to the scantlings and properties of the stiffened panel members, which include the plate, web, and flange. For convenience, the parameter for each parameter is normalized, yielding four non-dimensional parameters: plate slenderness, web slenderness, flange slenderness, and overall slenderness. The plate

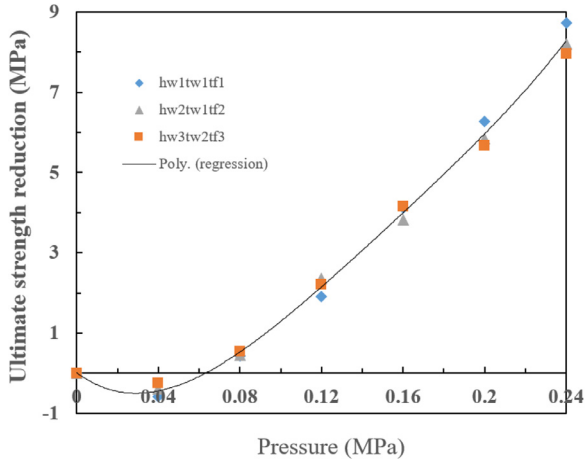

Fig. 16. Ultimate strength changes due to an increase in pressure loads. (For interpretation of the references to color in this figure legend, the reader is referred to the web version of this article.)

slenderness is kept constant based on the typical plate thickness of a tank in an oil tanker ship. The web, flange, and overall slenderness are calculated by using the case configurations that are listed in Table 2, with a span-over-bay ratio between three and six. The equations to calculate the slenderness parameters are listed in Eqs. (9)–(11).

$$\beta_{web} = \frac{h_w}{t_w}\sqrt{\frac{\sigma_Y}{E}}, \tag{9}$$

$$\beta_{flange} = \frac{0.5b_f}{t_f}\sqrt{\frac{\sigma_Y}{E}}, \tag{10}$$

$$\beta_{overall} = \frac{b}{\pi r}\sqrt{\frac{\sigma_Y}{E}}. \tag{11}$$

r is radius of the gyration, which is calculated as $\sqrt{I/A}$. The obtained ultimate strength reduction is plotted versus the web, flange, and overall slenderness, resulting in Fig. 17a–c. The influence of the parameter is assessed through the r-square value of the regression line. A low r-square value indicates that there is a small correlation between the targeted and input parameters, whereas a high r-square value indicates that the targeted parameter is sensitive to changes in the input parameter.

The r-square values in Fig. 17a and 17b are very small, implying a weak relationship between web and flange slenderness and ultimate strength reduction. However, Fig. 17c shows that the r-square value is close to one, indicating that overall slenderness is a critical parameter. For clarity, a sensitivity analysis based on the regression method is used, resulting in the regression parameters that are listed in Table 4. The regression results show a high value of r-square and a small value of significance F, implying that the obtained coefficients of determination for each parameter are adequate to capture the tendency of ultimate strength reduction [44]. The P-values show that the ultimate strength reduction is affected only by the overall slenderness and web slenderness. Furthermore, the coefficient of determination signifies that the influence of overall slenderness is approximately seven times greater than the influence of web slenderness. The high standard error and P-values for flange slenderness indicate that the influence of flange slenderness is not significant.

The seawater tank is a novel structure of an OTEC plantship that is subjected to excessive pressure as a result of the sum of hydrostatic pressure due to the submerged condition of the tank, dynamic pressure due to ship motion, and dynamic pressure due to seawater circulation inside the seawater tank. This paper investigates the ultimate strength of the stiffened panel via

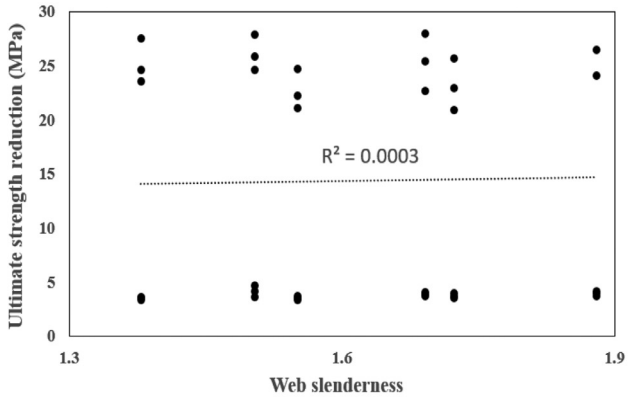

(a) Ultimate strength reduction vs web slenderness.

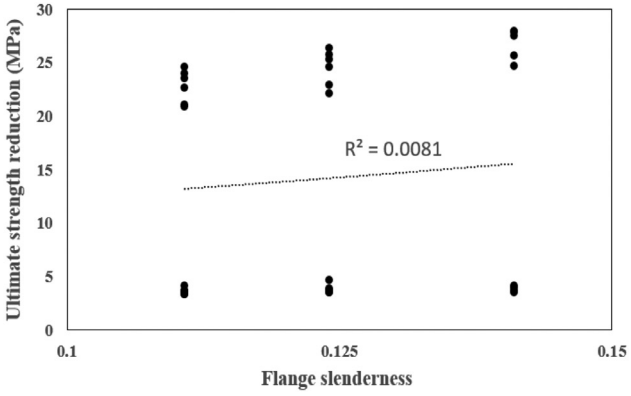

(b) Ultimate strength reduction vs flange slenderness.

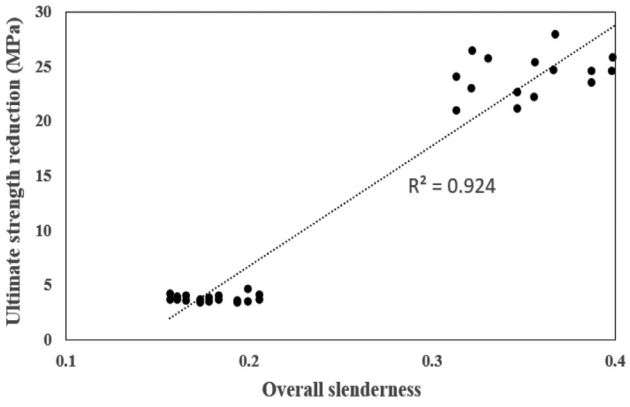

(c) Ultimate strength reduction vs overall slenderness.

Fig. 17. Scatter data of ultimate strength versus selected parameters. (For interpretation of the references to color in this figure legend, the reader is referred to the web version of this article.)

Table 4
Results of regression analysis.

Buckling mode	Indicators				
	Coefficient	Standard error	*P*-values	*R* square	Significance *F*
Intercept	-45.75	3.66	7.36392×10^{-14}	0.983	1.75828×10^{-28}
Overall slenderness	116.47	2.70	6.19583×10^{-30}		
Web slenderness	16.31	1.54	5.50658×10^{-12}		
Flange slenderness	9.13	9.93	0.364471822		

a non-linear FEA under the combined loadings of lateral pressure, transverse pressure, and axial compression to observe how the applied pressure affects the seawater tank structures. Before being used, the FEA procedures, which included geometrical modeling, meshing, and boundary conditions, were validated by comparing the results to the IACS-CSR code. The web height, web thickness, flange thickness, and span-over-bay ratio were varied, and their influence was evaluated by using sensitivity analysis.

The FEA results are in good agreement with those obtained by using IACS-CSR codes, implying that the FEA procedures have been confirmed. The results show that pressure reduces the ultimate strength of the stiffened panel. For relatively low pressures, the ultimate strength of the stiffened panel increased slightly and then decreased in a polynomial fashion with pressure increments. At 0.16 MPa of applied pressure, the ultimate strength decreased by approximately 4.1 MPa or approximately 1.5% for a span-over-bay ratio of 3 and approximately 22.4 MPa or approximately 7% for a span-over-bay ratio of 6. The result from the sensitivity study reveals that the overall slenderness influences the ultimate strength reduction the most.

The parameters will be increased in future research by covering the variation in plate slenderness and material properties. FEA will also be performed for the entire seawater tank structure while undesirable conditions such as geometric imperfection, welding residual stress, and so on are taken into account. Because the input parameters have a linear relationship with the targeted parameter, a simple regression method is sufficient for the sensitivity analysis in the present study. A more advanced method will be used for a more comprehensive analysis. Additionally, the imperfections due to manufacture and production processes include residual stress and geometrical imperfections. In the present study, the imperfection effect is focused on only for the geometrical imperfection. The effect of the residual stress on the ultimate strength of the stiffened panel will be analyzed in future work.

Declaration of Competing Interest

The authors declare that they have no known competing financial interests or personal relationships that could have appeared to influence the work reported in this paper.

CRediT authorship contribution statement

Yogie Muhammad Lutfi: Investigation, Formal analysis, Validation, Methodology, Writing – original draft. **Ristiyanto Adiputra:** Supervision, Conceptualization, Investigation, Data curation, Visualization, Writing – original draft, Project administration. **Aditya Rio Prabowo:** Supervision, Conceptualization, Writing – original draft, Writing – review & editing, Software, Funding acquisition, Project administration. **Tomoaki Utsunomiya:** Supervision, Conceptualization, Methodology, Writing – original draft. **Erwandi Erwandi:** Supervision, Conceptualization, Methodology, Visualization, Project administration. **Nurul Muhayat:** Supervision, Conceptualization, Methodology, Software, Writing – original draft.

Acknowledgments

This work is part of the OTEC research activity "Preliminary Design of a 5 MW OTEC plant: Study case in the North Bali" research grand DIPA-124.01.1.690505/2023 conducted by the Marine Renewable Energy Conversion Technology research group, Research Center for Hydrodynamics Technology, National Research and Innovation Agency (BRIN). Collaboration with the Laboratory of Design and Computational Mechanics, Universitas Sebelas Maret (UNS) is highly acknowledged.

References

[1] J.R. Marlon, X. Wang, M. Mildenberger, et al., Hot dry days increase perceived experience with global warming, Glob. Environ. Change. 68 (2021) 102247.
[2] K. Desmet, E. Rossi-Hansberg, On the spatial economic impact of global warming, J. Urban Econ. 88 (2015) 16–37.
[3] B. Cao, D. Bae, J.M. Sohn, et al., Numerical analysis for damage characteristics caused by ice collision on side structure, the ASME 2016 35th International Conference on Offshore Mechanics and Arctic Engineering, Busan, South Korea, June 18–24, 2016.
[4] M. Yusvika, A.R. Prabowo, D.D.D.P. Tjahjana, et al., Cavitation prediction of ship propeller based on temperature and fluid properties of water, J. Mar. Sci. Eng. 8 (2020) 465.
[5] M. Yusvika, A. Fajri, T. Tuswan, et al., Numerical prediction of cavitation phenomena on marine vessel: Effect of the water environment profile on the propulsion performance, Open Eng. 12 (2022) 293–312.
[6] A.R. Prabowo, T. Tuswan, R. Ridwan, Advanced development of sensors' roles in maritime-based industry and research: from field monitoring to high-risk phenomenon measurement, Appl. Sci. 11 (9) (2021) 3954.
[7] A.R. Prabowo, J.H. Byeon, H.J. Cho, et al., Impact phenomena assessment: Part I–Structural performance of a tanker subjected to ship grounding at the Arctic, MATEC Web. Conf. 159 (2018) 02061.
[8] P. Qin, More than six billion people encountering more exposure to extremes with 1.5°C and 2.0°C warming, Atmos. Res. 273 (2022) 106165.
[9] M. Salman, X. Long, G. Wang, et al., Paris climate agreement and global environmental efficiency: new evidence from fuzzy regression discontinuity design, Energy Policy 168 (2022) 113128.
[10] D.M. Prabowoputra, A.R. Prabowo, Effect of the phase-shift angle on the vertical axis Savonius wind turbine performance as a renewable-energy harvesting instrument, Energy Rep. 8 (2022) 57–66.
[11] Z. Arifin, S.D. Prasetyo, D.D.D.P. Tjahjana, et al., The application of TiO_2 nanofluids in photovoltaic thermal collector systems, Energy Rep. 8 (2022) 1371–1380.
[12] S.D. Prasetyo, A.R. Prabowo, Z. Arifin, The use of a hybrid photovoltaic/thermal (PV/T) collector system as a sustainable energy-harvest instrument in urban technology, Heliyon 9 (2023) e13390.
[13] E. Michael, D.D.D.P. Tjahjana, A.R. Prabowo, Estimating the potential of wind energy resources using Weibull parameters: a case study of the coastline region of Dar es Salaam, Tanzania, Open Eng. 11 (2021) 1093–1104.
[14] A.R. Prabowo, D.M. Prabowoputra, Investigation on Savonius turbine technology as harvesting instrument of non-fossil energy: Technical development and potential implementation, Theo. Appl. Mech. Lett. 10 (2020) 262–269.
[15] G. Wang, Y. Yang, S. Wang, Ocean thermal energy application technologies for unmanned underwater vehicles: A comprehensive review, Appl. Energy 278 (2020) 115752.
[16] J. Langer, J. Quist, K. Blok, Recent progress in the economics of ocean thermal energy conversion: critical review and research agenda, Renew. Sust. Energ. Rev. 130 (2020) 109960.
[17] R. Adiputra, T. Utsunomiya, Design optimization of floating structure for a 100 mw-net ocean thermal energy conversion (OTEC) power plant, the ASME 2018 37th International Conference on Ocean, Offshore and Arctic Engineering, Madrid, Spain, June 17–22, 2018.
[18] S.M. Masutani, P.K. Takahashi, Ocean thermal energy conversion (OTEC), in: J.H. Steele (Ed.), Encyclopedia of Ocean Sciences, Academic Press, Massachusetts, 2001, pp. 1993–1999.
[19] M. Faizal, M.R. Ahmed, Experimental studies on a closed cycle demonstration OTEC plant working on small temperature difference, Renew. Energ. 51 (2013) 234–240.
[20] C. Bernardoni, M. Binotti, A. Giostri, Techno-economic analysis of closed OTEC cycles for power generation, Renew. Energ. 132 (2019) 1018–1033.
[21] A. Giostri, A. Romei, M. Binotti, Off-design performance of closed OTEC cycles for power generation, Renew. Energ. 170 (2021) 1353–1366.
[22] R. Adiputra, T. Utsunomiya, J. Koto, et al., Preliminary design of a 100 MW-net ocean thermal energy conversion (OTEC) power plant study case: Mentawai Island, Indonesia, J. Mar. Sci. Technol. 25 (2020) 48–68.
[23] J. Herrera, S. Sierra, A. Ibeas, Ocean thermal energy conversion and other uses of deep sea water: a review, J. Mar. Sci. Eng. 9 (2021) 356.
[24] J. Langer, J. Quist, K. Blok, Upscaling scenarios for ocean thermal energy conversion with technological learning in Indonesia and their global relevance, Renew. Sustain. Energy Rev. 158 (2022) 112086.
[25] J. Langer, C. Infante Ferreira, J. Quist, Is bigger always better? Designing economically feasible ocean thermal energy conversion systems using spatiotemporal resource data, Appl. Energy 309 (2022) 118414.
[26] R. Adiputra, T. Utsunomiya, Stability analysis of free hanging riser conveying fluid for ocean thermal energy conversion (OTEC) utilization, the ASME 2019 38th International Conference on Ocean, Offshore and Arctic Engineering, Glasgow, Scotland, UK, June 9–14, 2019.
[27] R. Adiputra, T. Utsunomiya, Stability based approach to design cold-water pipe (CWP) for ocean thermal energy conversion (OTEC), Appl. Ocean Res. 92 (2019) 101921.
[28] R. Adiputra, T. Utsunomiya, Linear vs non-linear analysis on self-induced vibration of OTEC cold water pipe due to internal flow, Appl. Ocean Res. 110 (2021) 102610.
[29] R. Adiputra, T. Utsunomiya, Finite element modelling of ocean thermal energy conversion (OTEC) cold water pipe (CWP), the ASME 2022 41st International Conference on Ocean, Offshore and Arctic Engineering, Hamburg, Germany. June 5–10, 2022.
[30] R. Hisamatsu, T. Utsunomiya, Coupled response characteristics of cold water pipe and moored ship for floating OTEC plant, Appl. Ocean Res. 123 (2022) 103151.
[31] R. Hisamatsu, R. Adiputra, T. Utsunomiya, Experimental study on dynamic characteristics of fluid-conveying pipe for OTEC, the ASME 2022 41st International Conference on Ocean, Offshore and Arctic Engineering, Hamburg, Germany, June 5–10, 2022.
[32] R. Hisamatsu, T. Utsunomiya, A study on coupled behavior analysis and position keeping system for OTEC plantship and cold water pipe, J. Jpn. Soc. Nav. Archit. Ocean Eng. 32 (2020) 193–207 (in Japanese).
[33] D.E. Cavrot, Economics of ocean thermal energy conversion (OTEC), Renew. Energ. 3 (1993) 891–896.
[34] R.H. Yeh, T.Z. Su, M.S. Yang, Maximum output of an OTEC power plant, Ocean Eng. 32 (2005) 685–700.
[35] G.C. Nihous, L.A. Vega, Design of a 100 MW OTEC-hydrogen plantship, Mar. Struct. 6 (1993) 207–221.
[36] L. Martel, P. Smith, S. Rizea, et al., Final technical report, 30 May 2012, United States, 2012.
[37] K.N. Anyfantis, Ultimate strength of stiffened panels subjected to non-uniform thrust, Int. J. Nav. Archit. 12 (2020) 325–342.
[38] H. Ohtsubo, Y. Sumi, in: Proceedings of the 14th International Ship and Offshore Structures Congress, Elsevier Science, Amsterdam, 2000.
[39] R. Adiputra, T. Yoshikawa, E. Erwandi, Reliability-based assessment of ship hull girder ultimate strength, Curve. Layer. Struct. 10 (2023) 20220189.
[40] ABAQUSAnalysis User's Manual, Version 6.14, Dassault Systemes Simulia, Inc., 2014.
[41] IACS-CSRCommon Structural Rules For Bulk Carriers and Oil Tankers, International Association of Classification Societies, London, United Kingdom, 2022.
[42] M. Fujikubo, T. Yao, M.R. Khedmati, et al., Estimation of ultimate strength of continuous stiffened panel under combined transverse thrust and lateral pressure Part 1: Continuous plate, Mar. Struct. 18 (2005) 383–410.
[43] M. Fujikubo, M. Harada, T. Yao, et al., Estimation of ultimate strength of continuous stiffened panel under combined transverse thrust and lateral pressure Part 2: Continuous stiffened panel, Mar. Struct. 18 (2005) 411–427.
[44] S. Mohanty, R. Codell, Sensitivity analysis methods for identifying influential parameters in a problem with a large number of random variables, WIT Press, Southampton, 2003.